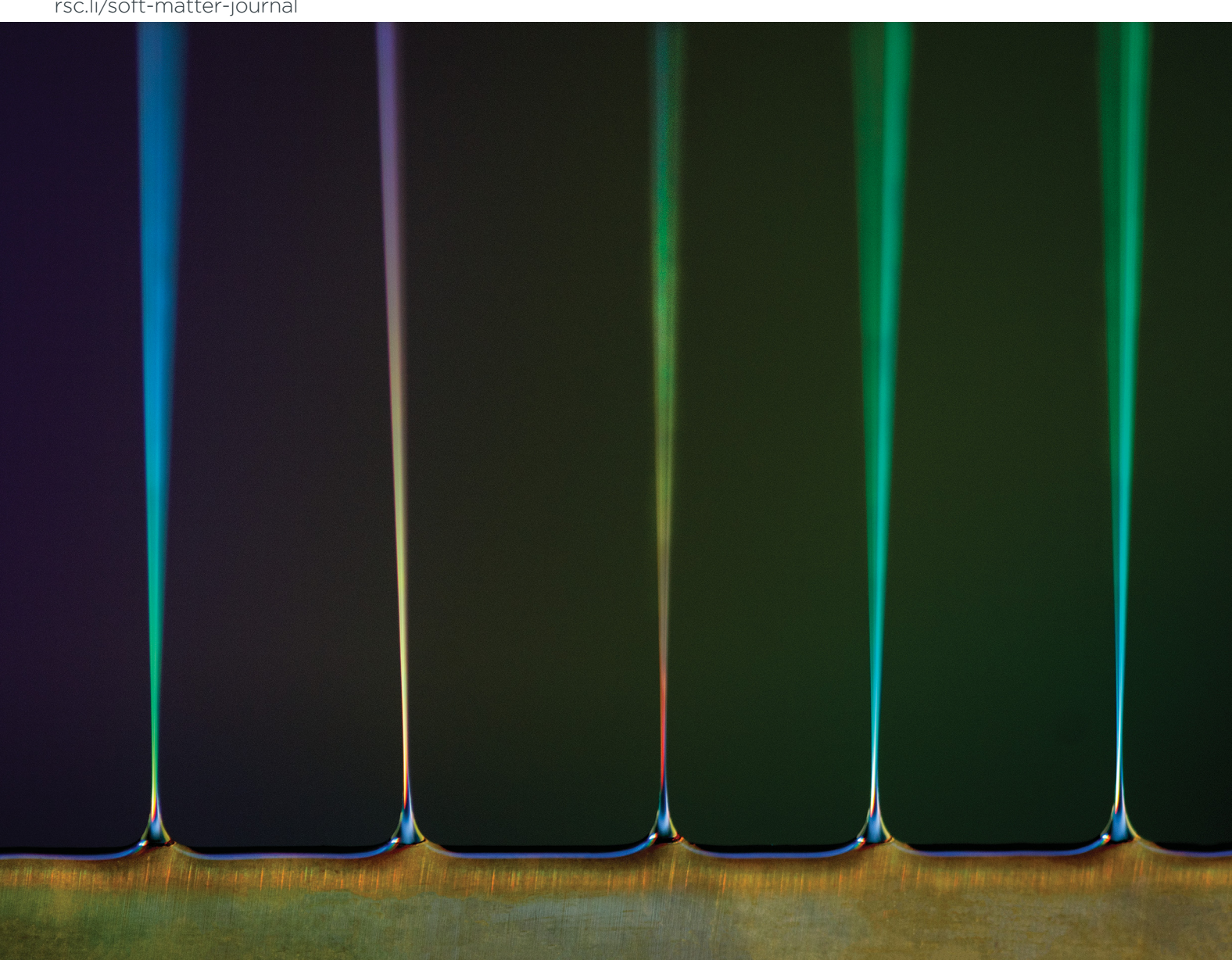
Volume 17 Number 41 7 November 2021 Pages 9249-9542

Soft Matter

rsc.li/soft-matter-journal



ISSN 1744-6848



PAPER

Jason R. Bochinski, Laura I. Clarke et al. Increasing ionic conductivity within thermoplastics via commercial additives results in a dramatic decrease in fiber diameter from melt electrospinning

Soft Matter



PAPER View Article Online
View Journal | View Issue

Increasing ionic conductivity within



Cite this: *Soft Matter*, 2021, **17**, 9264

in a dramatic decrease in fiber diameter from melt electrospinning†

thermoplastics via commercial additives results

Neelam Sheoran, Brent Boland, Samuel Thornton, Jason R. Bochinski ** and Laura I. Clarke ** **

Polyethylene melt conductivity was increased by adding a commercial anti-static agent, which resulted in a 20× decrease in electrospun fiber diameter and formation of a significant fraction of sub-micron diameter fibers. Two polyethylene formulations and varying additive concentrations were utilized to span the parameter space of conductivity and viscosity. The key role of conductivity in determining the jet radius (which sets the upper limit on the fiber size) is discussed in the context of fluid mechanics theory and previous simulations. Parameters which affect the conversion of the liquid jet to a solid fiber and the pertinent theory are outlined. An "unconfined" experimental configuration is utilized to both avoid potential needle clogging and enable direct observation of important characteristic length scales related to the interaction of the fluid and the applied electric field. In this approach, the fluid spontaneously forms an array of cone perturbations which act as stationary "nozzles" through which the mobile fluid flows to form the jet. The experimental data and theory considerations allow for a holistic discussion of the interaction between flow rate, viscosity, conductivity, and the resultant jet and fiber size. Information about the fluid viscosity and conductivity gained by observing the electrospinning process is highlighted. Schemes for theoretically predicting the cone-jet density, cone size, and flow rate are compared to experimental results.

Received 28th July 2021, Accepted 7th September 2021

DOI: 10.1039/d1sm01101d

rsc.li/soft-matter-journal

1. Introduction

Polymeric fibers are utilized in a wide variety of high societal impact applications such as wound dressings, water and air filters, and tissue scaffolds.^{1–5} Solvent-free nano- and meso-scale diameter fibers made from mechanically-strong thermoplastic polymers would be particularly valuable for many of these products. Such small fibers result in material with a very high surface-to-volume ratio and ample open space, facilitating high efficiency and long lifetime without clogging for filtration applications,^{6–11} as well as enabling cells to organize into tissues in an environment which is morphologically similar to that in nature for biomedical applications.^{12–15} Solvent-free nanofiber production eliminates concerns of trace solvent contamination in the final product and the negative human health and environmental consequences of using solvent in manufacturing. Use of high molecular weight, highly-entangled commercial

Department of Physics, North Carolina State University, Raleigh, NC 27695-8202, USA. E-mail: jason bochinski@ncsu.edu, laura clarke@ncsu.edu

polymers would ensure the resultant fibers have sufficient mechanical strength for higher pressure applications like filtration. Yet creating nanofibers directly from molten substances is problematic due in part to the high viscosity of polymer melts;^{3,16} this is particularly true for highly-entangled mechanically-strong materials. Electrospinning^{12,17-20} is a common technique to fabricate nanofibers, which in principle can use any entangled fluid. However, in practice, melt electrospinning has been strikingly unpopular: fewer than 6% of electrospinning scientific publications appearing in the last decade specifically address melt systems, 21 with the vast majority utilizing polymer solutions. As previously reported,²² some of the challenges with melt electrospinning can be addressed by replacing the traditional single metal needle through which a highly-viscous melt must be pumped with an unconfined configuration^{23–27} (e.g., a thin film of molten polymer on a flat metal plate). Jets spontaneously form on the sharp-edged plate, which eliminates clogging, enables many simultaneous jetting sites, and allows control of the jet size via tuning of the melt properties and electric field strength.

In this work, the fundamental relationships that underlie electrospinning of low conductivity, high viscosity polymer

[†] Electronic supplementary information (ESI) available. See DOI: 10.1039/d1sm01101d

Paper Soft Matter

melts (i.e., the melts formed by thermoplastics) are discussed. A particular focus is the underexplored role of low innate ionic conductivity. Electrospinning relies on the fluid having a moderate level of mobile ions: when an electric field is applied, ions move under the influence of the field, causing surface charges. This charged fluid then experiences a force due the electric field and/or charge repulsion, which ultimately propels it towards the collector. 28,29 When utilizing solution-based electrospinning, there are multiple potential ion sources; however in an additive-free molten thermoplastic the only ions present are due to chain defects or unintentional thermal degradation. All commercial thermoplastics have proprietary additive packages which might include antioxidants or other thermal stabilizers to prevent degradation, as well as whitening agents. 30,31 Such small molecule additives, which are introduced to serve different purposes, are most likely the serendipitous origin of ions which make melt electrospinning of these systems possible. The conductivity created by these sources is usually not measured nor optimized.

In this work, the ionic conductivity of polyethylene (the most common commodity thermoplastic worldwide) is altered, demonstrating that increasing the melt conductivity to levels typically found in solution-based electrospinning results in a 20× decrease in fiber diameter. This outcome, verified for two polyethylene formulations with significantly different physical properties, highlights that ionic conductivity is an overlooked fundamental characteristic which strongly affects electrospinning outcomes. Measuring and altering ionic conductivity enables a clearer delineation of the challenges in melt electrospinning, determining the various roles that high viscosity, lack of solvent loss, and low ion concentration and motion play in producing larger diameter fibers. By incorporating a readily-available, inexpensive commercial thermoplastic additive (e.g., an antistatic agent) at a low doping level, significant increase in molten ionic conductivity and concurrent decrease in fiber diameter was accomplished. We present measurements of ionic conductivity and viscosity as a function of temperature, describe changes in the electrospinning process, including cone size and cone-jet density, and apply theoretical analysis to explain alteration of each pertinent length scale including the resultant fiber size.

2. Results and discussion

2.1 Selection of materials and material properties

Polyethylene was selected as a target material because despite its ubiquitous commercial presence, it is rarely used for melt electrospinning.32-35 However, linear low-density polyethylene (LLDPE) is often utilized in microfiber form and has good mechanical properties (e.g., ASPUN is designed for fiber applications). Two different LLDPE formulations were utilized: ASPUN 6850a (ASPUN) has a moderate viscosity and contains a standard additive package while DNDA 1082 (DNDA) is a specialty formulation with a minimal additive package and a lower viscosity. Fig. 1 summarizes viscosity and conductivity measurements versus temperature for the two materials.

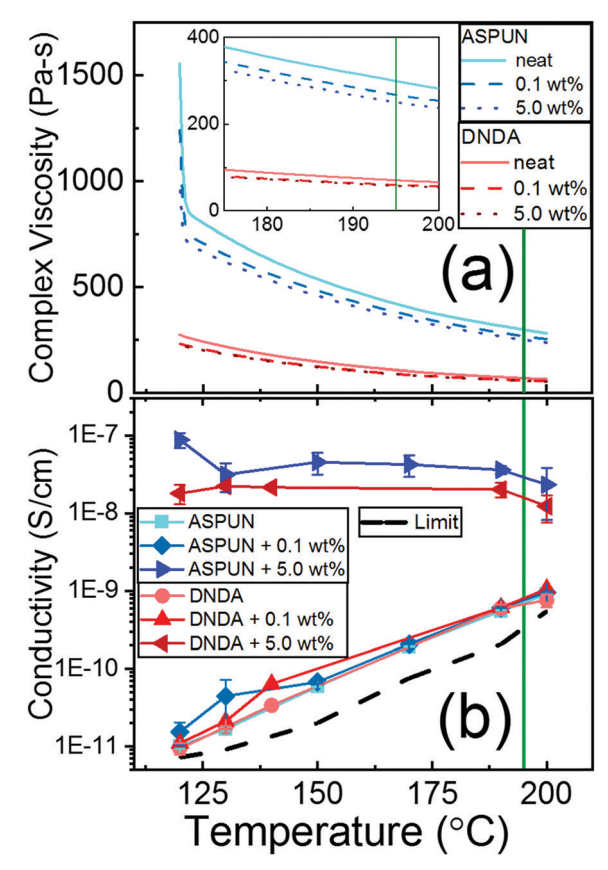


Fig. 1 (a) Viscosity as a function of temperature for ASPUN (blue data) and DNDA (red data) with 0.0, 0.1, and 5.0 wt% FA38 additive (solid, dashed, and dotted lines), respectively. Inset: A magnified view of region 0-400 Pa s and 175-200 °C. (b) Ionic conductivity as a function of polymer melt temperature for ASPUN (blue data; square, diamond, right-facing triangle symbols) and DNDA (red data; circle, triangle, left-facing triangle symbols) with 0.0, 0.1, and 5.0 wt% FA38 additive, respectively. The green vertical lines indicate the approximate polymer temperature used during the electrospinning process (~195 °C).

At 195 °C - the temperature used for electrospinning in this work – the viscosity of DNDA is $\sim 25\%$ that of ASPUN (Fig. 1a). The data was taken with decreasing temperature, thus the sudden increase at ~ 120 °C is due to polymer solidification. At the working temperature, the two unmodified polyethylene formulations (i.e., as received from the manufacturer) have similar conductivity values $\sim 7 \times 10^{-10} \text{ S cm}^{-1}$ (Fig. 1b). For comparison, the conductivity of solutions utilized for electrospinning typically falls in the range 10⁻⁶-10⁻⁴ S cm⁻¹; e.g., 4-6% (w/w) polyethylene oxide/water solution, which is a common nanofiber-forming, electrospinning fluid, 26,27 has a conductivity of $\sim 8 \times 10^{-5} \text{ S cm}^{-1}$.

To controllably increase the electrical conductivity of the LLDPE melts, the anti-static agent Hostastat FA38 (FA38) was utilized as a dilute ionic supplement. Using such a commercially-available additive, which was designed to be homogeneously incorporated into thermoplastics avoided chemical incompatibility or ineffective mixing between the melt and additive. Conventional antistatic agents generally combine hydrophobic and hydrophilic (e.g., phosphate and

Soft Matter

fatty acid esters) structures, and work by migrating to the surface of the polymer material in order to absorb water and ions from the air and improve the surface conductivity. This process may be a portion of the conductivity effect pertinent in this work, with bulk conduction due to ions likely also contributing. Ionic conductivity measurements temperature at 0.0, 0.1 and 5.0 weight percent (wt%) FA38 loading for the two LLDPE formulations are presented in Fig. 1b. Focusing on the data at 195 °C (Fig. 1, vertical green line) which is most pertinent for electrospinning, the DNDA [ASPUN] melt conductivity increased by $\sim 20 \times [\sim 40 \times]$ from 6.8×10^{-10} [7.3 \times 10 $^{-10}$] S cm $^{-1}$ as-received to 1.6 \times 10 $^{-8}$ [3.0 \times 10⁻⁸] S cm⁻¹ at the 5.0 wt% FA38 loading level. The dashed black line represents the measurement lower limit (due to the electrode) as a function of temperature. Fig. 1a shows the complex viscosity as a function of temperature for ASPUN and DNDA with 0.0, 0.1, and 5.0 wt% FA38 additive. The change in viscosity due to the additive is less than 20%. Within measurement error, we observed no change in surface tension (Section 2.2) or viscosity versus shear rate (Section 4.6) due to the additive; thus, our analysis focuses on the melt properties of conductivity and viscosity.

2.2 Spontaneous fingering to form cone-jets

The unconfined electrospinning apparatus, electric field pattern generated, and coordinate system utilized for this work are described in detail in Experimental methods. Polymer melt resides on a grounded, heated horizontally-oriented plate with a sharp edge. A nearby vertically-oriented plate serves as a collector and is held at a large negative voltage. The electric field pattern generated has a maximum magnitude at the sharp plate edge. After voltage is applied, the edge of the polymer melt film extends slightly ($\sim 300-800 \mu m$) past the plate edge in the direction towards the collector; we refer to this length scale as the x-extension. The nominal thickness of the polymer melt on the source plate is 1.8 mm. When voltage is applied, the thickness of the fluid extending past the plate edge is in the range of 200-600 μm (referred to as the y-extension). The extension lengths are smaller for the lower viscosity case, as discussed in Section 2.3.1. As further discussed below, the x- and y-extensions are part of a series of characteristic length scales that describe how the fluid is affected by the electric field, which also includes the characteristic cone size and the jet size and length. These quantities depend on the melt ionic conductivity.

The cone-jet initiation process occurs as follows: Ions within the melt experience forces due to the applied electric field, which leads to an excess of positive charges accumulating near the leading edge of the fluid. The charged melt near the edge of the plate expands, moving in the direction of the applied field (i.e., toward the collector). Surface tension works against such an expansion and the resultant instability causes the polymer melt to spontaneously finger to form many small protrusions, which ultimately transition into fiber forming cone-jets.²²⁻²⁷

This process is illustrated in Fig. 2 for the as-received polyethylene formulations.

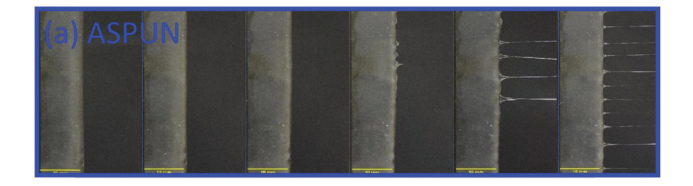




Fig. 2 Top down view of a sequence of photographic images of the spinning plate edge during the formation of protrusions and jets. The time sequence starting from t = 0 s, with images taken every 60 seconds (15 seconds) respectively, from left to right for ASPUN (DNDA). The scale bar represents 1 cm in each image.

The process of fingering and then cone-jet formation begins with a spontaneous fluctuation of the expanded fluid. As a result, both the time between application of the applied field and appearance of the first finger perturbation and the time required to reach the steady-state number of cone-jets are viscosity-dependent. The approximate time for the first finger perturbation to occur^{22,36} is given as:

Time for first pertubation =
$$\left(\frac{2\eta}{h^2}\right) \frac{27\gamma^2}{4\varepsilon_0^3 E^6}$$
, (1)

where h is the film thickness (i.e., y-extension), η is the viscosity, E is the electric field at the location where fingering begins, and γ is the surface tension. (Eqn (1)) (varying only by a co-factor of 12 versus 13.5) can also be derived by analogy with Rayleigh-Taylor instabilities,³⁷ substituting the electric force for gravity, and identifying h as a capillary length (see Section 2.3.1) which establishes relationships between h, γ , and E.

For instance, at the working electrospinning temperature of 195 °C, the viscosity of DNDA and ASPUN are 70 \pm 2 and 300 \pm 9 Pa s, respectively. After field application, the first finger perturbation for neat DNDA formed within 30 \pm 4 seconds while this process took 112 \pm 5 seconds for neat ASPUN. A comparison of experimental and theoretical values for the time to first perturbation is presented in Fig. 3. For theoretical calculations, the y-extension (h) was determined by imaging (after jet formation as discussed below) and the simulated electric field value used was from this y-extension and $1.3\times$ the x-extension measured at steady state, which is consistent with visual observations prior to, and during, the spontaneous fingering process. Thus the fluid edge pulls back slightly in the x direction after cone-jet formation. For theoretical calculations throughout this work, the viscosity values are those at 195 °C with a shear rate of 2.5% and a surface tension value of γ = $33.1 - 0.0390 \times T$ (°C) mN m⁻¹ with T = 195 °C is used.³⁸

After the protrusions form and organize, a steady-state is reached in which the cone-jets are approximately evenly spaced over the length of the plate and the x- and y-extensions are **Paper** Soft Matter

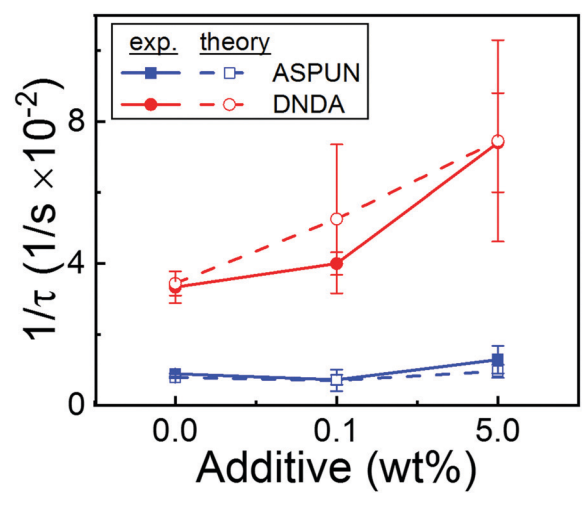


Fig. 3 Inverse average time to spontaneous perturbation formation at the plate edge $1/\tau$ as a function of additive FA38 wt% for two different formulations of LLDPE. Solid lines with filled symbols (dashed lines with open symbols) are experimental (theoretical, eqn (1)) $1/\tau$ values for ASPUN (blue square symbols) and DNDA (red circle symbols), respectively.

similar in size. A summary of the jet number as a function of time, including the steady state values is presented in Fig. 4.

The characteristic spacing λ between two cone-jets can be predicted using the equation^{22,36}

$$\lambda = \left(\frac{3\pi}{\varepsilon_0}\right) \frac{\gamma}{E^2},\tag{2}$$

where E is the electric field at the location of the fluid edge in steady state. Eqn (2) arises from determining the wavenumber where the growth rate (a generalization of eqn (1)) for perturbations is maximized. (Again, this expression (with a co-factor of $2\pi\sqrt{2}$ versus 3π) can also be derived using an analogy with Rayleigh-Taylor instabilities³⁷ and substituting the gravity force with electric force.) Theoretical estimates, using simulated electric field values at the experimentally observed x- and y-extensions are compared with experimental values in Fig. 4c; the agreement is good. For the neat polymer, the experimental (theoretical) λ values for DNDA and ASPUN are 4.19 \pm 0.15 mm $(4.15 \pm 0.21 \text{ mm})$, and $5.32 \pm 0.40 \text{ mm}$ $(5.47 \pm 0.58 \text{ mm})$, respectively. The physics of this initial process was described in more detail in previous works. 22,23,26 These experiments both demonstrate the early phase of the electrospinning process and confirm that the surface tension is not significantly altered by addition of the additive.

Additional characteristic length scales

Parameters such as electrical conductivity *K*, viscosity, flow rate O, surface tension, and electric field strength combine to determine the characteristic size of each feature of the electrospinning process: jet-to-jet spacing, cone width, x- and y-extension length, jet width, jet length, and ultimately, the final fiber size, as summarized in Fig. 5. In this section, mathematical expressions (utilizing previous treatments^{37,39,40}) for each additional pertinent length scale, along with the flow rate, beginning at the plate edge

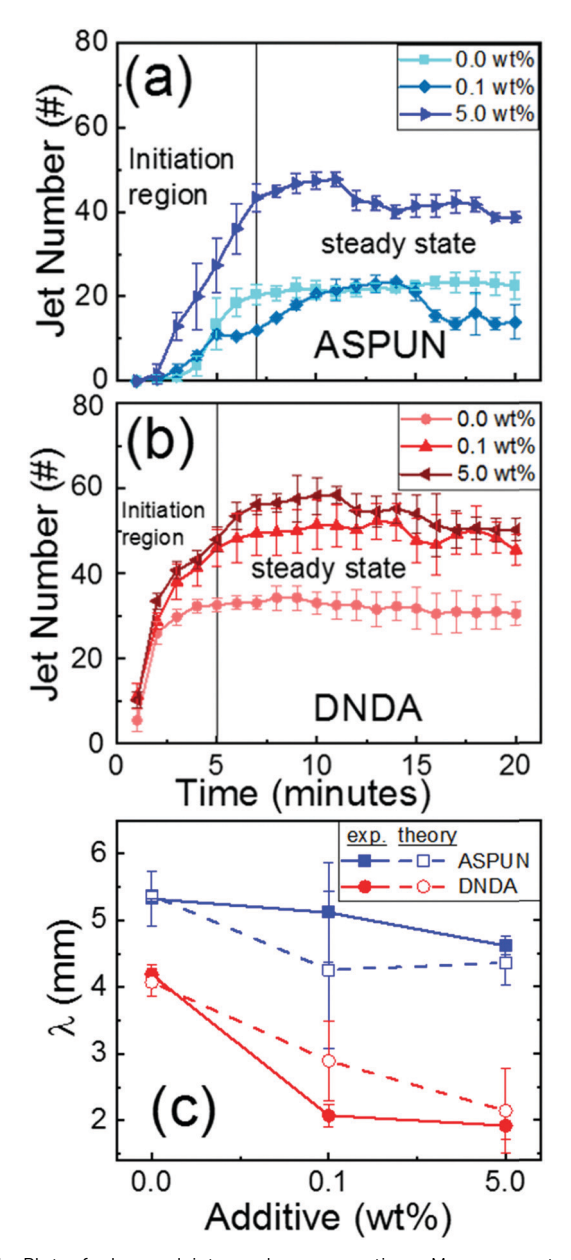


Fig. 4 Plot of observed jet number versus time. Measurements were performed by counting the number of jet sites every minute using video images for (a) ASPUN (blue data; square, diamond, right-facing triangle symbols) and (b) DNDA (red data; triangle, circle, left-facing triangle symbols) with 0.0, 0.1, and 5.0 wt% FA38 additive, respectively. The polymer melt temperature was held at 195 $^{\circ}$ C and -45 kV was applied to the collector. (c) Steady state values for each case with experimental data (filled symbols) compared to theoretical values (open symbols) from eqn (2).

and moving outward, are presented, discussed, and connected to experimental data.

2.3.1 Capillary length - understanding the fluid position on the plate and the cone width. The x- and y-extensions are similar to a meniscus formed by the fluid on the plate. In a classic meniscus,37 the size is related to the capillary length $\kappa_{\text{gravity}}^{-1} = \sqrt{\gamma/\rho g}$ where ρ is the mass density and g is the acceleration due to the gravity. The capillary length is the

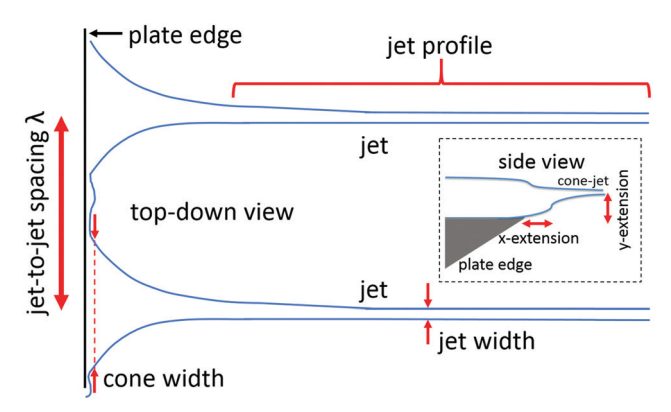


Fig. 5 Schematic depiction of the characteristic length scales in the melt electrospinning process from a top-down and side view perspective,

distance over which the force of gravity (due to the small mass) is negligible and thus capillary forces (i.e., those associated with surface tension) dominate. It can also be interpreted as a screening length: that is, the distance needed for the fluid to relax to a flat sheet moving away from a disturbance (e.g., the plate). An analogous approach can be utilized for the present experiment where the balance is between electric and capillary forces. Balancing the capillary and electric pressures (in direct analogy with the gravity derivation)³⁷ is $\gamma/\kappa^{-1} = \sigma E = \varepsilon_0 E^2$ (where σ is the surface charge density, the boundary condition $E_{\rm out}$ – $E_{\rm in} = \sigma/\varepsilon_0$ has been used, and complete screening of the electric field $E_{in} = 0$ is assumed), which results in

$$\kappa^{-1} = \frac{\gamma}{\varepsilon_0 E^2}.$$
(3)

Using the electric field at the observed x- and y-extensions and the known surface tension results in capillary length values which match the observed extensions (Fig. 6a). Thus, the data is consistent with eqn (3). Thinking physically, when the electric field has just been applied, the thickness of the film on the plate is 1.8 mm, which results in a capillary pressure of around 10 N. (The gravity capillary length is ca. 1.7 mm; thus gravity effects should be minimal.) The electric pressure (i.e., pressing outward towards the collector) is >80 N. Thus, as a consequence the fluid will move forward and thin. Thinning increases the capillary pressure (and, due to the experimental configuration utilized here, moving forward in the +x direction decreases the electric field). At the stationary point, the two pressures balance, which sets the x- and y-extension values. Using order of magnitude calculations, the assumption (based on experimental observations) that x- and y-extension values are similar at the final fluid edge location, and the known dependence of the electric field, this point occurs around 400 μm, which matches well with the experimental results (Fig. 6a).

Melts with higher conductivity and lower viscosity have systematically lower x- and y-extensions. We find that the experimental x- and y-extension values depend on η to a power of ca. 0.3 to 0.7. The change in x- and y-extensions has a weaker

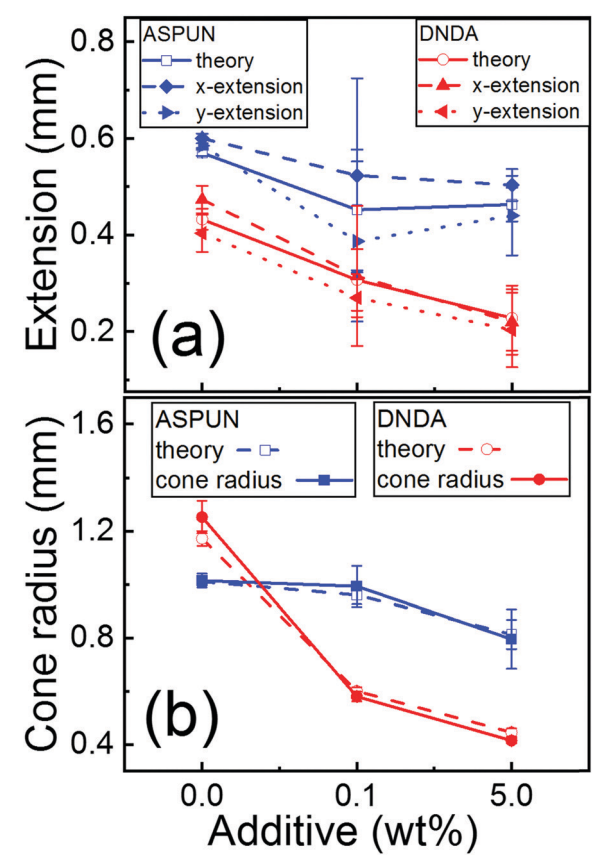


Fig. 6 (a) Position of the fluid edge relative to the plate edge (i.e., x-extension and y-extension) as a function of additive loading wt%. Experimental values (filled symbols) are measured for x- (diamond (ASPUN) and triangle (DNDA) symbols) and y-extensions (right-facing triangle (ASPUN) and left-facing triangle (DNDA) symbols), while theoretical values (open symbols) (square (ASPUN) or circle (DNDA) symbols) are calculated from eqn (3) using the electric field simulation value at the observed x- and y-extension location. (b) Cone width as a function of FA38 loading wt%. The different PE formulations are ASPUN (blue data) and DNDA (red data), with experimental values (filled symbols) and theoretical values (from eqn (3), open symbols) respectively.

dependence on conductivity, varying as K to the power of -0.1 to -0.3.

The stationary cone region around each jet can also be interpreted as a meniscus, where in this case the disturbance is the motion of the fluid in the jet region. Thus, the cone radius can also be estimated by the capillary length (see eqn (3)) with E the electric field at the terminal end of the cone (which is approximately $1.5 \times$ the cone radius). The comparison between the experimental data and theoretical estimates of the cone widths are presented in Fig. 6b.

Finally, identifying the y-extension as a capillary length, enables a re-examination of eqn (1), the time to first perturbation. Using $h \approx \gamma/\epsilon_0 E^2$ enables the simplification to time $\approx 27\eta h/2\gamma$. γ/η is the characteristic fluid velocity^{39,40} and the time is proportional to the capillary length, divided by this characteristic velocity. Because surface tension is relatively constant and the dependence of h on conductivity is weak, this simplification indicates that melt viscosity has the strongest effect on the perturbation time:

for the example case discussed in Section 2.2, a 4.3-fold increase in viscosity decreases the time by a factor of 3.7. The influence of the conductivity will occur in decreasing the capillary length, which results in a faster time (see Section 2.7). The capillary length also appears in eqn (2), where its classic identification as related to the inverse characteristic wavenumber $(\kappa^{-1})^{37}$ leads to $\kappa \sim 2\pi/\lambda \text{ or } \lambda \sim 2\pi\kappa^{-1}.$

2.3.2 Jet radius, jet length, and flow rate. While capillary lengths and cone-jet spacing provide useful visual evidence of changes in conductivity, the jet width has a direct impact on the ultimate fiber diameter, serving as the upper limit. The jet size for a viscous fluid is given by:

$$r_{\rm jet} = r_{\rm cross} = \frac{\eta^{\frac{1}{12}} Q^{\frac{1}{3}} \varepsilon_0^{\frac{1}{6}}}{\frac{1}{K^{\frac{1}{4}} E^{\frac{1}{6}}}},\tag{4}$$

with *E* is the electric field at the "cross-over" point as discussed below. 39,40 Eqn (4) results from a particular model in which flow Q is pushed through a circular hole (having radius a) in a flat plate and the electric field is uniform; however, this expression can be more generally applied. In this model and associated detailed simulations, near the source plate current is initially generated by volumetric flow (i.e., ions moving with the fluid) however, as the jet develops, ions move to the surface and the primary current mode becomes surface convention. The "jet radius" is identified as the crossover point r_{cross} where these two types of current are the same order of magnitude. Although the process is continuous, to simplify the discussion, for x (i.e., the coordinate direction that connects the source and collector plates) values less than this crossover point, one can think of the cone as transforming into a jet. For x values greater than this point, the jet is transforming into a fiber. The x value where the crossover occurs (the "jet length") is estimated by:

$$\ell_{\rm jet} = x_{\rm cross} \sim \frac{\eta^{\frac{1}{3}} Q^{\frac{1}{3}}}{\varepsilon_0^{\frac{1}{3}} E^{\frac{2}{3}}},$$
 (5)

where E is the electric field at the crossover point, as in eqn (4). Thus, when considering r(x), $r(x_{cross}) = r_{cross}$. For the viscous, low conductivity fluids where eqn (4) is applicable, x_{cross} is a reasonable distance from the plate edge: for the conditions explored in this work, 2-3 mm, where visually the cone has transitioned into a nearly parallel-sided jet. In practice, when applying eqn (4) and (5) to experimental data r(x), an iterative approach was utilized to self-consistently determine $r_{\rm cross}$ and x_{cross} , which both depend on the value of E at the location

From this analysis, we determined that the co-factor for eqn (5) is approximately 3 for the conditions utilized in this work. The process of charge transport to the surface is driven by the electric field; because the electric field decreases with distance in our apparatus, this process is elongated over the model prediction. Fig. 7a summarizes the agreement between experimental data and theoretical estimates of the jet radius $r_{\rm cross}$ and length $x_{\rm cross}$.

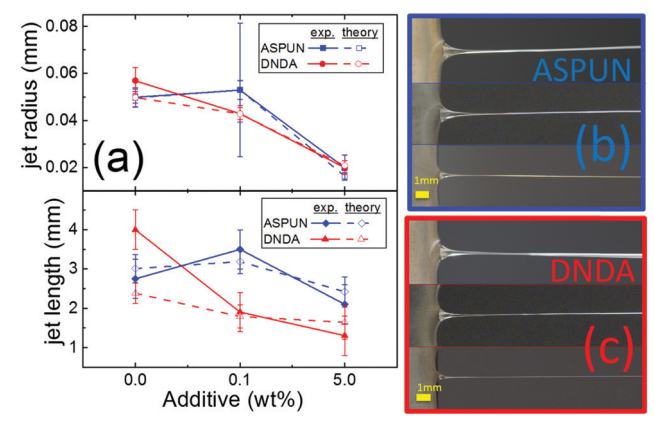


Fig. 7 (a) Measured experimental values (filled symbols) for the characteristic jet radius r_{cross} and length x_{cross} compared with theoretical predictions (open symbols) from eqn (4) and (5) for ASPUN (blue data) and DNDA (red data), respectively. As discussed in the text, $x_{cross} \sim a$. For this data group, we find $x_{cross} = 1.5a$ on average. Images of the jets at different additive loading levels 0.0, 0.1, and 5.0 wt% from top to bottom for (b) ASPUN and (c) DNDA.

Because flow rate has a large role in determining jet size and, in an unconfined electrospinning configuration, is itself determined by the electric field, Q was modelled by applying classical fluid theory.³⁷ In the lubrication approximation, which is valid for viscous systems at small size scales (i.e., thin films), the average fluid velocity goes as the film thickness squared times the pressure difference per length divided by the viscosity, with a co-factor of 1/3.37 This model invokes a thin film supported on a solid substrate with fluid motion parallel to the substrate due to different pressures (e.g., at the two ends of the substrate). The velocity is zero at the fluid-substrate interface and maximized at the free surface, resulting in a quadratic velocity profile perpendicular to the flow direction. For a conejet, pressure is associated with the electric field as $\varepsilon_0 E^2$, and flow proceeds in the x-direction. A core of fluid moves through the interior of the cone with the exterior region remaining largely stationary (i.e., as though the fluid has formed a nozzle which is immobile except within the innermost region). Considering this interior jet and moving outward radially at a fixed x value, the velocity is maximum at the radial center and almost zero at the transition into the stationary cone. Thus, the radius of the interior jet is analogous to the film thickness. We denote this length scale as a because it is the equivalent of the orifice

size in the theory³⁹ utilized to derive eqn (4) and (5). Thus, v =

 $\frac{a^2}{3\eta}\frac{\varepsilon_0 E^2}{L}$ where ν is the average velocity, and L is a characteristic distance over which the pressure varies (e.g., the cone-jet length). Using the electric pressure and the deviation in this pressure with x from the simulation results, and multiplying the velocity by the cross-sectional area results in:

$$Q = 2\pi\varepsilon_0 E \frac{a^4 dE}{3\eta dx},\tag{6}$$

where the electric field and derivative are taken from the

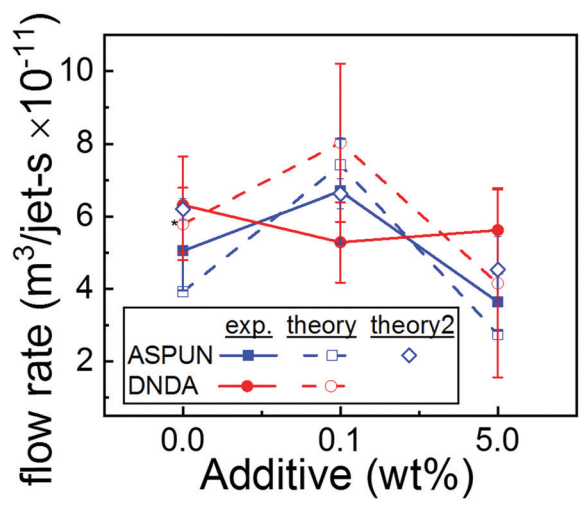


Fig. 8 Comparison of experimental data (filled symbols) and theoretically calculated (open symbols) flow rate from egn (6) as a function of FA38 loading wt% for ASPUN (blue squares) and DNDA (red circles), respectively. Letting $a = 0.75r_{cone}$ ($a = 0.40r_{cone}$) gives the open (starred open) symbol theoretical fit. For ASPUN, the order of magnitude theory, $Q \propto \pi a^2 \frac{\gamma}{n}$ is also plotted (open blue diamonds).

simulation at the x- and y-extensions. The effective radius ais the only unknown and it must lie between the jet and cone radii.

The experimental Q data was well fit by utilizing a = 0.4to 0.8× the experimentally determined cone radius. Fig. 8 summarizes the results for experimental and predicted Q with a value of $a = 0.75r_{\text{cone}}$ for all cases except the neat DNDA data, which requires $a = 0.4r_{cone}$. Thus for most cases, roughly 75% of the cone width is moving fluid with the outer 25% serving as an orifice for the mobile fluid. For DNDA (and to a lesser extent DNDA + 0.1 wt% FA38) which has both low viscosity and low conductivity, the mobile portion of the cone is smaller. Previous workers^{39,40} have defined the ratio of the residence time of fluid in the cone-jet transition region to the charge relaxation time, $\varepsilon\varepsilon_0/K$ where ε is the dielectric constant (ca. 3 for a

polymer melt). This ratio $\frac{\pi\eta^{1/2}}{K^{1/2}\varepsilon\varepsilon_0E}$ relates to the number of electric

relaxation cycles (i.e., the time needed for charge to re-arrange) that occur while the fluid moves through the jet. Low ratio values (which occur for DNDA neat and DNDA + 0.1 wt% FA38) were associated with a quantities that were a smaller fraction of the cone radius. This is consistent with fast flow (low viscosity) and slower charge transfer due to low conductivity.

The observed flow rate is almost constant as the conductivity and viscosity are changed. Combining the most basic form for

 $Q = \frac{\pi a^4 \varepsilon_0 E^2}{3\eta}$ with eqn (6) or examining the experimental data

indicates that related quantities L and $\ell_{\rm jet}$ are proportional to a, which is itself a fraction of r_{cone} . Thus both a and L are likely set by capillary lengths (see Section 2.3.1) with the only difference being the particular electric field value used in eqn (3). Considering a and L proportional and substituting the capillary length from eqn (2) results in $\nu \propto \gamma/\eta$ (which also appears in the discussion at the end of Section 2.3.1) and $Q \propto \pi a^2 \frac{\gamma}{n}$. This

approach results in a reasonable fit, as shown in Fig. 8 for ASPUN ($a = 0.75r_{cone}$, open blue diamonds) Note that this expression has no explicit dependence on E. Considering the dependence of a on viscosity, this simplified form helps explain why Q is relatively constant despite changes in conductivity and viscosity, as discussed further in Section 2.3.3.

It is useful to re-visit eqn (4) and (5), which contain both Q and E, and substitute eqn (6) which also relates these two quantities. This results in

$$r_{\rm jet} = r_{
m cross} \sim \frac{\varepsilon_0^{1/2} a E^{1/2}}{K^{1/4} \eta^{1/4}}, \quad \text{and } \ell_{\rm jet} = x_{
m cross} \sim a,$$
 (7)

where the dimensional approximation that $\frac{dE}{dx} \sim \frac{E}{a}$ and the assumption that E at the crossover point (the E in eqn (4) and (5)) is some fraction of E at the plate edge (which is the Equantity in eqn (6)) have been used. These results are discussed in detail in the following section.

2.3.3 The uniquely useful role of conductivity in setting the jet radius. Examining eqn (4), the parameter with the largest influence on the jet radius is the flow rate. Q is dependent on the cross-section area (a^2) and the velocity, which increases with the driving force (proportional to E) and decreases with the viscosity. However, as discussed above, the experimental values for the flow rate (with similar E field values, Fig. 8) reveal that 5 of the 6 conditions explored in this work have the same flow rate to within error, even though the two formulations of polyethylene have viscosities that differ by a factor of 4. To better understand this observation, we can examine the interplay between a and viscosity. In particular, a has a hidden dependence on viscosity, as it is proportional to the cone radius which is set by the capillary length, which experimentally increases with viscosity $(a \sim \eta^{0.3-0.5})$. Considering the order of magnitude estimate $Q \sim$ $a^2\gamma/\eta$ (i.e., the cross-sectional area times the characteristic velocity) or the more detailed form in eqn (6), where the electric field also has a hidden dependence on η (i.e., as viscosity decreases, the capillary length decreases, and thus E increases), and substituting for a, reveals that the flow rate is almost viscosity independent, as observed experimentally. Examining the jet radius form in eqn (7), shows the same effect: the quantity a/ $\eta^{0.25}$ is almost constant with viscosity, and thus the jet radius is relatively independent of viscosity. Therefore, if one is seeking to decrease the jet radius by reducing the flow rate, then the viscosity is not a useful parameter in an unconfined system. Experimental results summarized in ESI,† Fig. S1 confirm that viscosity has no predictive effect on jet size. DNDA melts with viscosity values in the range of 60-70 Pa s and ASPUN melts with η ranging from 250–300 Pa s display almost identical $r_{\rm iet}$ values of 20-60 µm and 20-50 µm, respectively. For the neat cases where the conductivity is almost identical, but the viscosity varies by $4\times$, the DNDA and ASPUN jet radii vary by <15%.

Decreasing E may decrease the flow rate and thus also r_{iet} , which is desirable for nanofiber formation. However, sufficient decrease in E will lead to the pattern of cone-jets collapsing and extinguish the electrospinning process; thus this is not a productive approach.

Such analysis makes the unique utility of the conductivity clearer. Increasing K will decrease the jet radius directly. Examining eqn (7), it has no other significant counterbalancing effects: increased K will also decrease a but this is only a weak dependence, which mitigates a potential increase in E as result of the fluid pulling closer to the plate edge. Experimental data bears out this analysis. Fig. S1b (ESI†) shows r_{iet} as a function of measured conductivity: the downward trend with conductivity raised to the power -0.25 (as in eqn (7)) is evident. Tuning K to alter r_{iet} is also fundamentally more experimentally achievable than the alternative of decreasing E or increasing η to decrease the flow rate, particularly with the facile repurposing of preexisting additives. Characteristic images of the cone-jet regions near the plate edge are shown for each three experimental cases for ASPUN (Fig. 7b) and DNDA (Fig. 7c) with progressively higher additive wt%. It is clear that upon increasing conductivity all features are smaller including the jet radius.

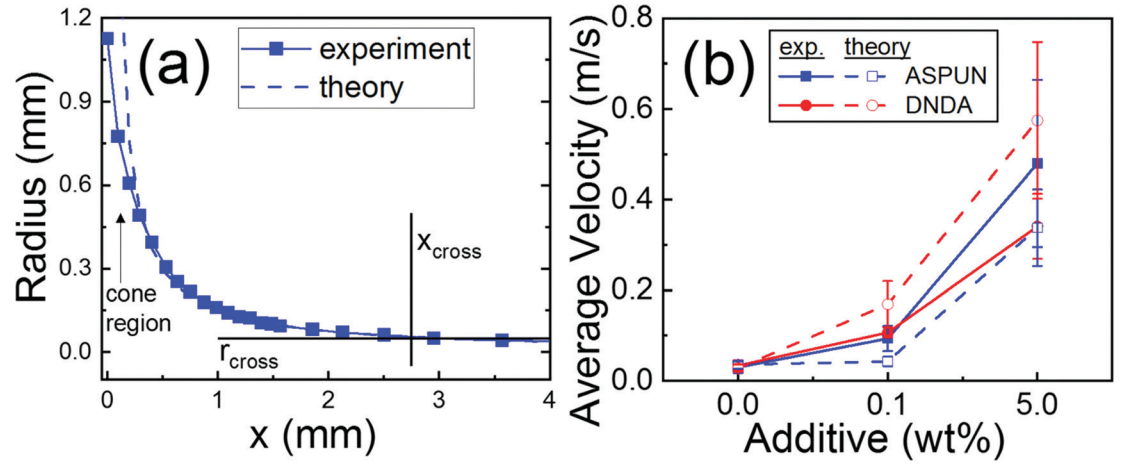
2.3.4 Fiber diameter. The same simulation and theory approach^{39,40} for viscous melts that results in eqn (4) and (5), provides a form for the radius as a function of x, sufficiently far from the plate edge. This should at a minimum be applicable for $x > x_{\text{cross}}$ (i.e., past the crossover point), which is the region in which the jet transforms into the final fiber.

$$r(x) \sim \left(1 + \sqrt{1 + \frac{24IE\eta}{\pi} \frac{2}{\gamma^2}}\right) \frac{\gamma Q}{2IEx} \approx \left(1 + \sqrt{1 + \frac{24}{\pi} \frac{e^{\frac{1}{3}} \frac{7}{\eta^6} K^{\frac{1}{2}} Q^{\frac{2}{3}} \frac{5}{3}}{\gamma^2}}\right) \times \frac{\gamma Q^{\frac{1}{3}}}{2\epsilon_0^{\frac{1}{3}} \eta^{\frac{1}{6}} K^{\frac{1}{2}} E^{\frac{5}{3}} x} \sim \frac{\eta^{\frac{5}{12}} Q^{\frac{2}{3}}}{\epsilon_0^{\frac{1}{6}} K^{\frac{1}{4}} E^{\frac{5}{6}} x}}$$
$$\sim \frac{\epsilon_0^{1/2} E^{1/2} a^2}{\eta^{1/4} K^{1/4} x},$$
(8)

where the total current I was estimated from the surface current at the cross-over point, as in the original work. The surface charge density at the cross-over point (involved in the derivation of eqn (4) and (5)) $\sigma \sim \varepsilon_0^{1/2} E^{1/2} \eta^{1/4} K^{1/4}$, results in $I \sim \varepsilon_0^{1/3} \eta^{1/6} K^{1/2} Q^{2/3} E^{2/3}$. This derivation assumes a constant electric field and thus the presence of a co-factor is expected, which again is approximately 3 for the experimental conditions in this work with E in eqn (8) set to the value at the cross-over point. Note that the co-factor for r(x) and that for $x_{\rm cross}$ cancel resulting in an unchanged expression for $r_{\rm cross}$ (i.e., eqn (4)). Substituting the expression for Q (i.e., eqn (6)), results in the final term.

Eqn (8) indicates that the fiber radius should decrease roughly as $\frac{1}{x}$, where x is the distance from the source plate. This prediction can be compared to experimental results in several ways. Fig. 9a shows a characteristic jet profile of r versus x taken from analysis of optical images. Such data is quantitatively reliable relatively close to the plate edge; further out, loss of focus or movement of the fiber during the shutter time results in feature broadening. Experimental data from all six cases was generally consistent with the $\frac{1}{2}$ form and could be fit using the penultimate term in eqn (8), with the only adjustable term being the co-factor which was in the range of 2-3. As shown in the figure, near the plate edge, the cone-jet is dominated by the cone. After this region, the jet theoretical prediction could be matched to the experiment through the cross-over point before loss of focus and jet motion affected the experimental data. For the theoretical fit in Fig. 9a, the average experimental fiber radius of 13 µm would be expected to occur at x = 11 mm, which is reasonable, given visual observations of the experiment.

To further experimentally test the r(x) model, informal velocimetry was utilized where imperfections (e.g., air bubbles)



(a) A characteristic experimental jet radius (blue squares, blue line) compared with theoretical predictions (blue dashed line) from eqn (8) for ASPUN. Near the plate edge, the cone-jet is dominated by the cone formula as expected. The $\frac{1}{x}$ form for the jet is consistent with the data out to and beyond the cross-over point, here marked by the average x_{cross} (2.75 mm) and r_{jet} ($r_{cross} = 50 \mu m$). After ca. 4 mm, motion of the forming fiber and loss of focus make the experimental data unreliable. The theoretical curves is about 75% of that predicted by eqn (8) (with a co-factor of 3) for this condition, within the expected error, and reaches the predicted fiber size (i.e., 13 µm) at 11 mm. (b) Measured average velocities for each experimental case (filled symbols, solid lines) for ASPUN (blue data) and DNDA (red data) were compared with the theoretical equivalent case (open symbols, dashed lines).

in the melt were identified in video data and tracked to estimate the average speed of the fluid flow. (For additional details, see the Experimental methods section.) Because flow rate is a constant (i.e., there is no mass loss) as the fiber thins, the fluid velocity increases. Measured average velocities for each experimental case were compared with the theoretical average velocity, found by assuming a $\frac{1}{2}$ decrease in radius from the jet to the fiber, as shown in Fig. 9b. The agreement is good for the lower conductivity cases where speeds are relatively low and solidification (i.e., formation of the solid fiber due to cooling) occurs relatively close to the source plate (within 1-2 cm of the total working distance of 10 cm). For lower viscosity, higher conductivity cases, the velocity estimates are the same order of magnitude. In these cases, visual observations indicate that the fibers are at least semi-liquid upon arrival at the collector; however, the theoretical expression predicts hardening at the final fiber diameter much earlier (by ca. x = 3 cm). Thus experimentally the fiber is not thinning as rapidly as expected in the region far from the source plate, which is likely due to increased viscosity from cooling and/or decreased electric field (both of which affect the co-factor of $\frac{1}{2}$ in eqn (8)), as discussed further in Section 2.4.

Characteristic scanning electron microscopy images of the resultant electrospun fibers are presented in Fig. 10, along with histograms of the fiber diameter and the resultant average size. For DNDA (Fig. 10, right column), increasing conductivity (top to bottom rows) resulted in a decrease in fiber diameter

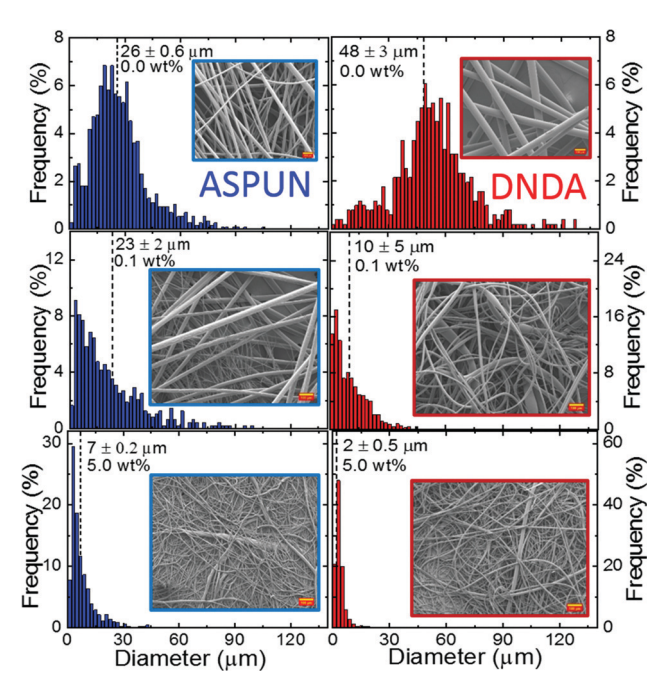


Fig. 10 Histogram graphs of melt electrospun fiber diameters for ASPUN (blue data, left column) and DNDA (red data, right column) as a consequence of increased additive loading wt% (top to lower row). In each graph, the inset is an SEM image of the fibers; scale bars in each graph represent 200 μm.

by 20× (i.e., from 48 \pm 3 μm to 2 \pm 0.5 μm). For the as-received DNDA (Fig. 10, right column, top row), melt electrospun fibers removed from the collector were thread-like with little observable fiber-fiber bonding, consistent with the relatively large fiber size and complete solidification before reaching the collector. After increased ionic conductivity via inclusion of the FA38 additive, the resultant fibers were visually cotton-like, with an average fiber diameter of $\sim 2 \mu m$. For higher viscosity ASPUN, the decrease in fiber diameter was $\sim 4\times$. These differences are discussed in the next section. ESI,† Fig. S2 shows an expanded view of the lower histogram panels of Fig. 10 for easier viewing. Increasing the melt conductivity results in a significant increase in fraction of fibers produced with sub-micron diameters: for example, for DNDA + 5 wt% FA38 20% of the fibers created were nanofibers, as compared with 0% for the neat DNDA.

2.4 The path from jet to fiber

As argued above, the jet radius, which sets the upper limit on fiber size, is a key parameter to understand and control when seeking to produce smaller fibers. As discussed in detail in Section 2.3.3, analysis and preliminary data show that ionic conductivity of the melt can be used in a practical sense to reduce jet size and the viscosity, perhaps surprisingly, is not an important parameter.

As discussed in Section 2.3.4, after the jet is established, the theoretical prediction indicates that jet/fiber diameter will continuously decrease while it remains pliable. To illustrate, the role of fluid parameters, we here discuss a few cases in detail. Summarized in Fig. 9a, as-received ASPUN has an average radius 50 μ m jet at x = 2.75 mm which produces a $4\times$ smaller fiber diameter (13.5 μ m), which if the $\frac{1}{x}$ form holds, occurs at x = 11 mm. Using eqn (8) (with a co-factor of 3) to theoretically predict the radius, velocity, and thus fluid transition time from x = 1 mm to the collector (with $r = r_{\text{fiber}}$ at and beyond x = 11 mm), results in a predicted transition time of 2.8 s, which matches well with the experimental value of 3.3 ± 1.4 s. This analysis indicates that the fiber was pliable for about 2 s (the time taken to reach x = 11 mm). The results and analysis for neat DNDA match similarly.

For ASPUN with 5.0 wt% FA38 loading, the cross-over jet radius is 20 μ m, occurring at x = 2.1 mm with a fiber diameter of 3.4 µm reached at 14.5 mm, and a transition time prediction of 0.29 s compared well with the experimental estimate of 0.21 ± 0.1 s. The flow rate for this case is about two-thirds that of the as-received ASPUN but the velocities are higher because the fiber/jet is smaller. The "draw ratio" $\frac{r_{\rm fiber}}{r_{\rm fiber}}$ for ASPUN with 5.0 wt% FA38 is again \sim 4, with the fiber staying pliable for ca. 0.2 s. We expect that the time to cool and solidify will be smaller for finer fibers due to the increase in fiber surface area.

Lower viscosity melts (DNDA) with larger draw ratios, and longer time to solidification reveal limitations of the prediction. Although transition time estimates match to within error and the model shows larger distances before

solidification (22 and 42 mm for 0.1 and 5.0 wt% FA38, respectively) as expected, the theory transition times are consistently lower than experiment, which indicates that thinning is slower than the theoretical limit. Experimentally, for the 5.0 wt% loading case, fibers appear to still be fluid when arriving at the collector which is x = 10 cm. Given the jet radius of 20 µm occurring at 1.3 mm, if the theory held, a fiber radius of ~ 200 nm is predicted, as opposed to the actual observed value of 1.2 μm. As expected, this discrepancy indicates that the thinning process is slower and more complex in the spatial region far from the plate edge. The maximum draw ratio (around 17) is achieved for this DNDA + 5.0 wt% FA38 loading case, which has similar jet diameter and transition time as ASPUN + 5.0 wt% but remains liquid for significantly longer, which may be reflective of its lower viscosity.

Thus while the jet size, which can be controlled by conductivity, sets the upper limit on the fiber size, dynamics within the elongation region (after x_{cross}) influence the final fiber radius. These include the temperature in that region, the fiber size (due to increased heat loss) and viscosity. While viscosity does not have a dominant effect on the jet size, it has more influence on the transition from jet to fiber. For instance, the highest conductivity ASPUN formulation is more than 2× the conductivity the equivalent DNDA case and forms a similar jet diameter but results in fibers 4× larger. This effect is likely due to the larger melt viscosity.

The role of the additive in increasing melt conductivity

Most neat ionic compounds are unlikely to be compatible with hydrophilic thermoplastic polymers. Thus, use of ion-containing additives, intended for other purposes but designed to incorporate into particular polymeric systems, was an important component of achieving this work.

A conductivity increase of 20-50× was achieved by incorporating the FA38 additive, which also resulted in a slight (<20%) decrease in melt viscosity. Conductivity reflects both the volume density of ionic charge and the ionic mobility, which can be impacted by viscosity. Estimating the maximum interaction between mobility and viscosity as an inverse linear relationship⁴¹⁻⁴⁴ indicates that the conductivity increase due to viscosity change should be proportionally small. Note that while the viscosity of the two formulations varies by $4\times$, their conductivities are almost identical for as-received and 0.1 wt% cases, and the highest conductivity is observed in the high viscosity LLDPE polymer (ASPUN) at 5.0 wt% additive loading. Thus, the dominant effect of additive doping appears to be relatively straightforward, that is, an increase in the number of mobile ions per volume.

Advantages of the open plate configuration

The high viscosity of polymer melts creates many practical challenges for electrospinning, including nozzle clogging and the need for high pressure pumping, when using "confined" or needle-based systems. 22-27 The unconfined configuration utilized here prevents these problems but also has tangible benefits for fundamental studies because the fluid location and

dynamics reveal order of magnitude information about fluid properties and the fluid-field interaction. We briefly discuss some examples below:

(1) As discussed at the end of Section 2.3.1, the time to first perturbation is most strongly influenced by viscosity (in a system where the polymer is unchanging and thus γ is constant) with time $\approx \eta h/\gamma$. To demonstrate this empirically, for the four cases where the conductivity is relatively constant (as-received and with 0.1 wt% FA38), the time to first perturbation can be well predicted by an empirical form of either (0.43 \pm $(0.05) \times \eta$ or $(0.10 + 0.02) \times \eta^{1.3}$. In the first case, the relatively weak dependence of h (the y-extension) on viscosity $(\eta^{0.3})$ is neglected; in the second, it has been included explicitly. The y-extension also has a weak dependence on conductivity $(h \sim K^{-0.2})$. Fitting the higher conductivity data (5.0 wt% FA38) with the first form results in a co-factor of 0.2-0.3, which is consistent with this K dependence: using the power of -0.2, a 20-50× increase in conductivity should result in a decrease in the co-efficient by a factor of ~ 2 , which is consistent with these numbers (0.43 goes to 0.22). This means that the time to the first perturbation can be utilized as a measure of viscosity.

(2) The location of the fluid edge relative to the plate (i.e., the x- and y-extension) is meniscus like, increases with viscosity (to the 0.3 power), and decreases weakly with conductivity (to the -0.2 power, see Section 2.3.1). Cone width has the same basic dependence on viscosity and conductivity, although it is correlated with the electric field at a different location (the apex of the cone), and thus is systematically larger (due to the lower field). As in most electrospinning configurations, a sharp feature (here, the plate edge) is utilized to maximize the electric field, which results in an inhomogeneous field with position; thus minute changes in the x- and y-extensions result in a change in the electric field and thus the jet-to-jet spacing

 $\lambda = \left(\frac{3\pi}{\varepsilon_0}\right) \frac{\gamma}{E^2}$. Both the x- and y-extensions and the jet-to-jet spacing are related directly to the capillary length $\gamma/(\varepsilon_0 E^2)$, however while the extension length scale is small ($\sim 400 \mu m$) and difficult to image (best viewed from the side of the plate), the jet-to-jet spacing has a co-factor of ~ 12 , making it an order of magnitude larger, is repeated multiple times along the plate edge, and is easily viewed from above. Thus, increased jet

density is an indication that the capillary length has decreased due to decreased viscosity, increased conductivity, or both, and thus the fluid now resides in a larger electric field.

As an example of obtaining information about viscosity and conductivity directly from visual observations, consider images of the early electrospinning process for DNDA with 0.0, 0.1, and 5.0 wt% FA38 loading in Fig. 11. The time to the first perturbation is similar in all cases (occurring between the third and fourth images), indicating that the viscosity is similar (which it is, varying by less than 20%). Compare these results to Fig. 1 where the viscosity varies by 4× and time increments in parts (a) and (b) also vary by $4\times$. The slight dependence of the time to first perturbation on conductivity is not easily quantified, even though the conductivity varies by 20× from as-received to 5.0 wt%.

Soft Matter

(a) 0.0 wt%

1cm

(b) 0.1 wt%

1cm

(c) 5.0 wt%

Fig. 11 Photographic images of the spinning plate edge (top down view) captured every 15 seconds for 8 consecutive images (left to right) showing the evolution of protrusions and jets formation for samples composed of (a) as-received DNDA and those with the addition of (b) 0.1 wt%, and (c) 5.0 wt% loading FA38. The scale bar represents 1 cm in each image.

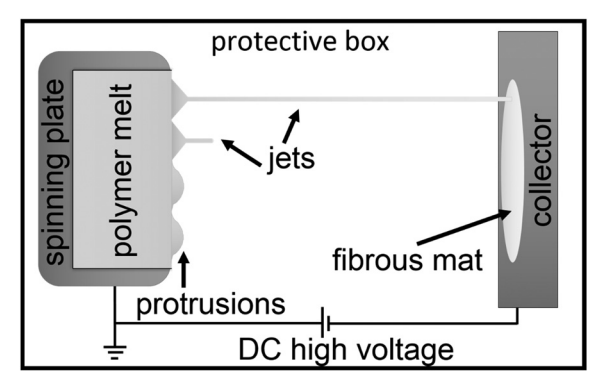


Fig. 12 Schematic diagram (top-down view): after application of high voltage the polymer melt on the horizontal metal spinning plate spontaneously forms protrusions, leading to jet creation and subsequent fibrous mat deposition on the metal collector located 10 cm from the plate edge. Note: The spinning plate rests on top of a hot plate which is not shown in the image for enhanced clarity.

However, looking at the last image in each sequence, it is clear that the jet density increases and the cone width decreases as the weight percent of additive increases. Having already established that the viscosity is relatively constant by observing the time to first perturbation, these changes can be attributed to an increase in conductivity. The average jet-to-jet spacing decreased by $\sim 2\times$ from 0.0 to 5.0 wt% FA38, which indicates that the capillary length also halved. This result is consistent with the known increase in conductivity by a factor of 20 ($20^{-0.2} = 0.55$).

3. Conclusion

The conductivity of polyethylene melts was increased by up to $50 \times via$ incorporation of a commercial anti-static agent which provided additional ions to facilitate smaller characteristic size

scales, including the meniscus size, cone width and jet width. The process by which a thin fluid film spontaneously forms an array of cone-jets in unconfined melt electrospinning was reviewed and the characteristic time to first perturbation described and connected to the fluid viscosity. In this process, the fluid extends beyond the plate towards the collector and this characteristic length scale (the x- or y-extension) is determined by the fluid viscosity and conductivity and connected to the capillary length. For lower viscosity or high conductivity, the extension length is smaller (e.g., the fluid end is closer to the plate edge); due to the inhomogeneous electric field created by the sharp plate edge, the electric field at this location is larger, leading to increased jet density. Cone size is also a capillary length and proportional to the observed extension lengths. An extensive discussion of the factors that determine the jet radius and an argument that increasing the conductivity is the most facile means to decrease characteristic jet size are presented. Jet size is a particularly important parameter because the fiber begins forming at the jet; thus smaller characteristic jet sizes should enable thinner fibers. A decreased flow rate will also decrease the jet radius, but in an unconfined electrospinning geometry (likely necessary for melt electrospinning due to high fluid viscosities), the flow rate is almost completely determined by the electric field and can be difficult to tune easily. In fact, in sampling a parameter space that included changing the viscosity by $4\times$ and the conductivity by $50\times$, the measured flow was constant to within a factor of 2. In addition, because the electric field is crucial to forming and maintaining the cone-jets, and thus enabling electrospinning, decreasing the electric field with the goal of decreasing flow rate will ultimately result in collapse of the cone-jet. The transition from jet to fiber is influenced by the distance the fluid travels after the jet and before the fiber solidifies. Thus, a second effect of narrower jets is higher fluid velocities at the jet, thus an ability to potentially travel further during the time before solidification and resultant formation of thinner fibers.

4. Experimental methods

4.1 Materials and characterization

Two grades of linear low-density polyethylene (LLDPE) were utilized: ASPUN 6850A (ASPUN) and DNDA 1082 NT 7 (DNDA) (Dow Chemical) with a melt temperature ($T_{\rm m}$) and melt flow index (MFI) of 131 °C, 30 g/10 min and 125 °C, 160 g/10 min, respectively. LLDPE pellets were cryo-ground (SPEX CertiPrep 6750 freezer-mill) to obtain a powder. Dynamic scanning calorimetry (DSC) (PerkinElmer Diamond DSC-7, 25 °C to 450 °C at 20 °C min⁻¹) confirmed melting points in the range 131–135 °C and 125–129 °C, with no substantial change observed after cryo-grinding or heating at 200 °C for 60 minutes. The anti-static agent Hostastat FA38 (FA38) (Clariant) was utilized as a dilute ionic supplement. Additive and polymer powder were physically mixed and stirred for approximately 5 minutes prior to use to achieve homogeneity.

4.2 Apparatus

The melt electrospinning apparatus (Fig. 12) consists of a machined aluminum source plate (base dimensions 16.25 \times 5×2.5 cm) with a replaceable tungsten carbide-tipped blade (Magnate PK0618T 15 \times 2.5 \times 0.3 cm) attached flush to the plate surface with countersunk screws to provide a consistent, sharp plate edge. The thin edge has a radius of curvature of ~21 µm as measured in a confocal laser scanning microscope (Keyence VKx1100). (See ESI,† Fig. S3 for a detailed drawing.) The source plate rests on a commercial hot plate (Fisher Scientific Type 1900) with the blade edge protruding by 0.4 cm. Before and after the electrospinning process, a type-K thermocouple (Omega) was inserted into the melt film to measure the temperature. The source plate is electricallygrounded using a copper metal rod attached to a thick aluminum braid. The aluminum collector (20 \times 30 cm, covered with removable aluminum foil) is located 10 cm from the source plate and held at a negative electric potential by a high voltage source (Glassman High Voltage Model FC60R2). The collector, source plate, and hot plate reside in an enclosure with cement board sides, a 1/4" tempered glass (United Plate Glass) top, and a removable polycarbonate viewing window on the front side. During experiments, the box is situated inside a chemical fume hood.

To initiate each experiment, the source plate is temporarily removed and the hot plate is set to temperature in order to warm the box interior. 10 gram of polymer powder (as-received or with additive) is uniformly spread over the source plate. After \sim 30 minutes when the enclosure interior reaches a steady state temperature of \sim 55 °C, the front window is briefly opened and the loaded source plate positioned on the hotplate. Once the enclosure is resealed, the polymer and source plate attain the desired equilibrium set temperatures (polymer melt ~195 °C; plate ~202 °C) within approximately 30 minutes. After an additional 5 minutes quiescent stabilization time, a mechanical handle temporarily engages the thermocouple onto the polymer melt surface to measure the temperature about 1 cm back from the source plate edge. Subsequently, a negative-polarity high voltage is applied to the collector, thereby initiating the electrospinning process and starting the experiment. Electrospinning continues for 20 minutes without any observed substantial decrease in polymer melt thickness. The measured DNDA and ASPUN LLDPE fiber fabrication rates were ca. 5.5, 6.6, and 7.7 g h⁻¹ and 2.1, 2.4 and 3.5 g h⁻¹, respectively for samples containing 0.0, 0.1 and 5.0 wt% FA38. Thus, the calculated mass loss ranged from 0.7-2.6 g.

4.3 Characterizing the electrospinning process and fiber morphology

Neat ASPUN and DNDA LLDPE experiments were initially performed under a range of temperature (160-210 °C) and high voltage (-41, -43, -45, -47 kV applied to the collector)conditions to optimize operating parameters. Subsequent electrospinning experiments using polymer with additive (0.0, 0.1 and 5.0 wt% FA38) were performed under the optimized

conditions with a high voltage of -45 kV and a polymer temperature of 190-200 °C. Both a camcorder and a highresolution camera (Sony, Model HDR-CX240 and Sony, Model a7R IV with Canon EF 180 mm f3.5L macro telephoto lens, respectively) separately observed the edge of the source plate (top and side views) to monitor the electrospinning process.

Data on size scales, number of jets versus time, fiber size, and the time to first perturbation is reported as an average with error the standard deviation of the average from four separate experiments. Image analysis was conducted using postprocessing software (Image-J) where jet number versus time was determined at one-minute intervals from single video frames. High resolution optical images were examined to measure the cone width and extension of the fluid film over the plate edge (x- and y-extension, see Section 2.2), as well as to quantify the jet/fiber radius as a function of distance from the source plate. Motion of the jets/fibers during the exposure time prevented clear visualization of the jets/fibers at distances further than 3-5 mm from the plate edge. Velocity estimates and measured diameters of the resultant fibers were utilized to extrapolate fluid behavior beyond this region. Fiber samples (retrieved from left, center and right regions of the collector) were obtained by fitting aluminum stubs with adhesive tabs into a wooden holder with equidistant separations, and pressing the stubs to the mat; thus enabling reproducible sampling locations from different experimental runs. To produce a conductive surface and reduce charging effects, stub-mounted samples were coated with ~60 nm of gold/ palladium alloy in a sputter coater (Quoron Technologies, S67620) at a rate of 7 nm min⁻¹. Subsequent fiber diameters, diameter distribution, and overall mat morphology were determined via scanning electron microscopy (SEM) imaging (Phenom FEI desktop SEM operating at 5 kV).

Average fluid velocity was estimated using an informal velocimetry approach. Jets which possessed a notable imperfection (e.g., such as a bubble or particle identified from video data) were monitored with screenshots to calculate the time for the observed distinctive feature to travel from the plate edge to the collector. For higher conductivity fluids, the video playback speed was reduced to ensure adequate time resolution. Multiple (i.e., typically 3-4) cases were identified for each experimental condition with the average velocity determined via dividing the distance by the observed time interval. Theoretical estimates of jet radius versus position were obtained by using the penultimate form in eqn (8) with the experimental values of flow rate, viscosity, and conductivity, the simulated electric field at the cross-over point (see Section 2.3.2) and a co-factor of 3. These theoretical curves matched experimental r versus x (the coordinate connecting the source plate and collector) data relatively well. The distance between the source plate and collector was divided into slices starting at x = 1 mm, and proceeding with 2.5 mm increments until 1 cm, and 1 cm increments thereafter until reaching the collector at x = 10 cm. Utilizing the theoretical jet radius *versus* position data and the experimental flow rate, the velocity at the beginning and end of each slice was determined. The transition

time for each slice was the length of the slice divided by the average of the initial and final velocities. The slice transition times were summed to find a total transition time and the average velocity was calculated, in direct analogy with the experimental value, by dividing the total distance by the total time.

4.4 Calculation of electric fields

Soft Matter

The electric field pattern within the electrospinning apparatus was simulated by a commercial modelling program (ANSYS electromagnetic desktop 2020). A three-dimensional electrostatic finite element analysis was employed with adaptive meshing. The initial mesh was generated using the TAU method with moderate mesh resolution and curvilinear meshing enabled while spatial detail was enhanced in areas of interest by specifying mesh operations on those geometries. The source plate edge was assigned a surface approximation mesh operation limiting the accepted normal angular deviation to 15°. A volume enclosing the path connecting the center of the plate edge and the collector center was set to have a maximum mesh length of 10 µm. The tetrahedral mesh was refined each pass by adapting the 30% highest error tetrahedrons until a desired percent energy error was reached; subsequently, the optimized final mesh had 7×10^6 tetrahedrons and 0.27% error in energy. Fig. 13 shows the result for an applied voltage of -45 kV. The coordinate system has an origin near the upper edge of one corner of the plate (see Fig. S3, ESI \dagger). The z direction is parallel to the plate edge, x is the direction along which spinning occurs, starting at the plate edge and continuing to the collector, and y is the direction opposite gravity that reflects the height of the fluid film on the plate edge.

4.5 Conductivity measurements

Conductivity measurements were performed (Hikoi IM3533-01 LCR meter) over the frequency range of 1 Hz-200 kHz and temperature range of 120-200 °C on ASPUN and DNDA melts having three different concentrations of the antistatic additive (0, 0.1 and 5 wt%). Measured values were verified with an ultraprecision capacitance bridge (Andeen-Hagerling 2700a) in the overlapping frequency range 50 Hz-20 kHz. Gold interdigitated electrodes (IDE) (Metrohm) with 125 digit pairs of 6750 µm length and a 10 µm gap residing on a rectangular glass substrate (2.2 \times 7.6 \times 0.7 cm in size) were UV-ozone cleaned for 30 minutes (Bioforce Nanosciences UV-Ozone Procleaner), followed by rinsing with isopropyl alcohol, and submersion for 12 hours in 1000:1 (toluene:dimethyl decyl chlorosilane) solution. The silane reacts with surface hydroxyl groups and replaces them with methyl and decyl groups, which results in a hydrophobic surface and reduces water contamination of the electrodes. After silanization, IDEs were rinsed with toluene, sonicated in methanol for 2 minutes, and stored in a closed container until use. Powder (polymer + additive) was placed on an individual IDE, heated on a hot plate to 140 °C, and then allowed to cool to form a polymeric film. Samples resided on a metal stage in a shielded probe station (Desert Cryogenics

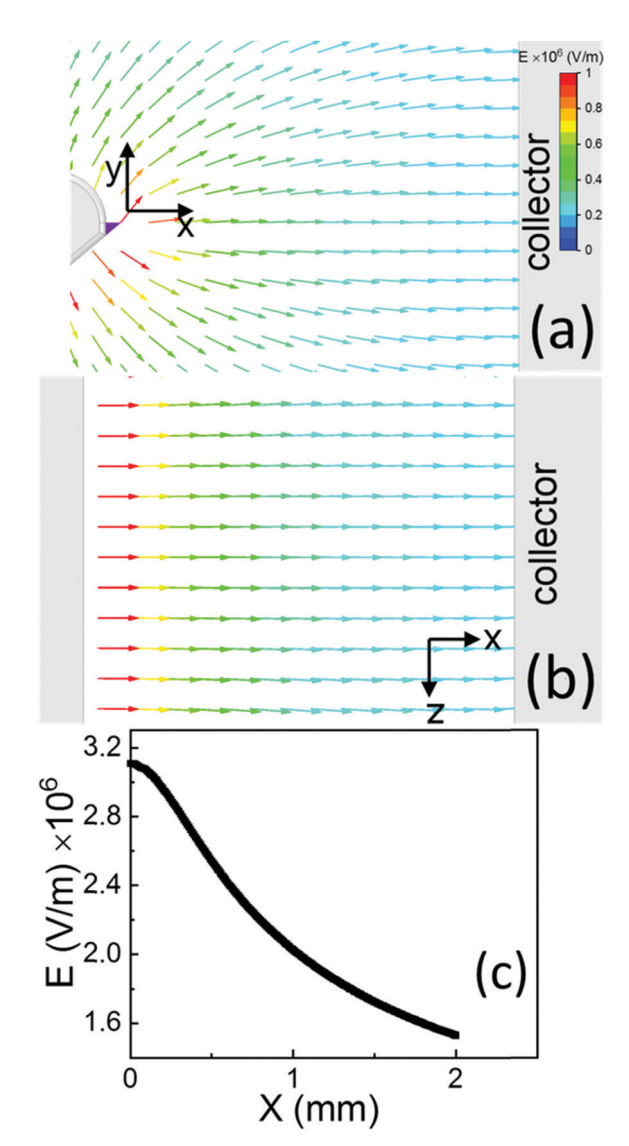


Fig. 13 Electric field simulation results viewed from (a) side, and (b) top-down perspectives, respectively, with the field amplitude color scale given above. The purple triangle in (a) indicates the blade edge where the polymer is placed. (c) The magnitude of the electric field at the center of the plate and a location of $y=380~\mu m$ (i.e., at the average location of the polymer surface where jets form) as a function of x, where the origin $x=0~\mu m$ is located at the plate edge. The distance from plate edge to the collector is 10 cm.

model #DC1472) for measurements under high-vacuum ($\sim\!10^{-5}$ torr) or ambient conditions.

Complex impedance as a function of frequency (AC test signal $0.1~V_{\rm rms}$) was measured and the ionic conductivity determined by fitting the data to a model circuit (Fig. 14). Nyquist plots were created (Zview version 3.2b software) for each temperature point using the full available frequency spectrum. RC models with a capacitor phasor element were used to fit Nyquist plot semicircles to obtain the bulk resistance values at zero frequency. Example data with fit are shown in Fig. 14a. A single parallel RC circuit was used for fitting samples with low ionic conductivities (*i.e.*, with single semicircle in Nyquist plot Fig. 14b) vs two parallel RC circuit in

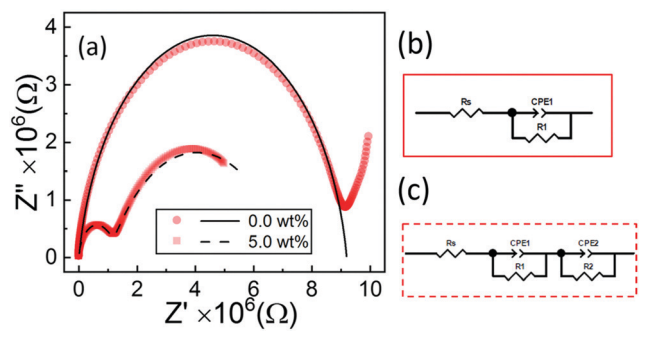


Fig. 14 (a) Experimental Nyquist plots (imaginary part versus real part of the complex impedance) for as-received DNDA (circles) and DNDA + 5.0 wt% FA38 (squares) at 200 °C. (b) A single RC circuit model was used to fit data from as-received and 0.1 wt% FA38 loading additive cases, and (c) a two parallel RC model circuit was used for data from 5.0 wt% additive melts, resulting in the fits shown as black lines (solid and dashed, respectively). Fitted R values from these curves were used to calculate the bulk resistance of the polymer melt sample.

series for higher conductivities (i.e., with two semicircles in Nyquist plot Fig. 14c). Final conductivity values, K (in S cm⁻¹), were calculated using $K = \frac{k}{R_{\rm B}}$ where k is the cell constant of IDE (in cm⁻¹) and $R_{\rm B}$ is the bulk resistance. The IDE cell constant was confirmed by measuring a liquid conductivity standard (potassium chloride in water with conductivity of 5 μS cm⁻¹, VWR) under ambient conditions. The measurement sensitivity limit is set by the background signal from the IDE, determined by measuring each IDE prior to use over the same frequency and temperature range (1 Hz-200 kHz and 120-200 °C, respectively). The limit varies with temperature and is $\sim 1 \times 10^{-11} \, \text{S cm}^{-1}$ at $T_{\rm m}$ and $\sim 2 \times 10^{-10} \, \text{S cm}^{-1}$ at 190 °C. The conductivity at 195 °C (i.e., the average measured polymer melt temperature during electrospinning) used in calculations is a linear extrapolation of the experimental values at 190 and 200 °C.

4.6 Rheology measurements

Rheology measurements were performed on polymer and additive mixtures (parallel plate PP25 on an Anton Paar MCR-302 rheometer). Molten samples 25 mm in diameter and 1 mm thick were measured at temperatures from 120-200 °C. Amplitude sweeps were performed to determine the viscoelastic regime for each sample, working at the temperature extremes and using constant angular frequency with varying shear strain (0.01-100%). Subsequent viscosity measurements were performed in this viscoelastic regime to minimize shear thinning for the given temperature range. Shear strain ranged between 0.1-5% at a constant frequency of 1 Hz. The viscosity used in theoretical calculations is the measured value at 195 °C at a shear rate of 2.5%. Viscosity versus shear rate was not altered by the presence of the additive.

Author contributions

Neelam Sheoran: methodology, investigation, formal analysis, writing - original draft; Brent Boland: methodology, investigation,

formal analysis; Samuel Thornton: methodology, investigation; Jason R. Bochinski: funding acquisition, supervision, writing review & editing; Laura I. Clarke: funding acquisition, conceptualization, supervision, formal analysis, writing - review & editing.

Conflicts of interest

There are no conflicts of interest to declare.

Acknowledgements

This research was supported by the National Science Foundation (NSF) (grant CMMI-1635113). Some measurements were performed in the NC State Physics Education and Research Laboratory (EaRL) as well as at the Analytical Instrumentation Facility (AIF) at North Carolina State University, which is supported by the State of North Carolina and the NSF (grant ECCS-1542015). The AIF is a member of the North Carolina Research Triangle Nanotechnology Network (RTNN), a site in the National Nanotechnology Coordinated Infrastructure (NNCI). The authors thank Ms Birgit Anderson for DSC measurements, Mr Hai Bui for precision machining of the spinning apparatus, and Prof. Russell Gorga for useful discussions. The authors also thank NC State libraries, the Department of Physics, and Dr Ryan Boland for use of cameras, the Nonwovens Institute at NC State University for polymer material, Clariant for providing Hostastat FA38, and Prof. Keith Weninger and Prof. Karen Daniels for use of equipment.

References

- 1 C. P. Barnes, S. A. Sell, E. D. Boland, D. G. Simpson and G. L. Bowlin, Nanofiber technology: Designing the next generation of tissue engineering scaffolds, Adv. Drug Delivery Rev., 2007, 59, 1413-1433.
- 2 S. Cavaliere, S. Subianto, I. Savych, D. J. Jones and J. Roziere, Electrospinning: designed architectures for energy conversion and storage devices, Energy Environ. Sci., 2011, 4, 4761-4785.
- 3 T. D. Brown, P. D. Daltona and D. W. Hutmacher, Melt electrospinning today: An opportune time for an emerging polymer process, Prog. Polym. Sci., 2016, 56, 116-166.
- 4 D. Liang, B. S. Hsiao and B. Chu, Functional electrospun nanofibrous scaffolds for biomedical applications, Adv. Drug Delivery Rev., 2007, 59, 1392-1412.
- 5 J. J. Xue, T. Wu, Y. Q. Dai and Y. N. Xia, Electrospinning and Electrospun Nanofibers: Methods, Materials, and Applications, Chem. Rev., 2019, 119, 5298-5415.
- 6 D. Lv, M. M. Zhu, Z. C. Jiang, S. H. Jiang, Q. L. Zhang, R. H. Xiong and C. B. Huang, Green Electrospun Nanofibers and Their Application in Air Filtration, Macromol. Mater. Eng., 2018, 303, 18.
- 7 X. Y. D. Ma, J. M. Ang, Y. F. Zhang, Z. H. Zeng, C. Y. Zhao, F. G. Chen, B. F. Ng, M. P. Wan, S. C. Wong, Z. B. Li, C. B. He and X. H. Lu, Highly porous polymer nanofibrous aerogels cross-linked via spontaneous inter-fiber stereocomplexation

and their potential for capturing ultrafine airborne particles, *Polymer*, 2019, **179**, 10.

Soft Matter

- 8 R. Purwar, K. S. Goutham and C. M. Srivastava, Electrospun Sericin/PVA/Clay Nanofibrous Mats for Antimicrobial Air Filtration Mask, *Fibers Polym.*, 2016, 17, 1206–1216.
- 9 R. Asmatulu and W. S. Khan, *Electrospun nanofibers for filtration applications*, Elsevier Science Bv, Amsterdam, 2019, pp. 135–152.
- 10 S. Zhang, N. A. Rind, N. Tang, H. Liu, X. Yin; J. Yu and B. Ding, Electrospun Nanofibers For Air Filtration, 2019, pp. 365–389.
- 11 R. S. Barhate and S. Ramakrishna, Nanofibrous filtering media: Filtration problems and solutions from tiny materials, *J. Membr. Sci.*, 2007, **296**, 1–8.
- 12 D. M. dos Santos, D. S. Correa, E. S. Medeiros, J. E. Oliveira and L. H. C. Mattoso, Advances in Functional Polymer Nanofibers: From Spinning Fabrication Techniques to Recent Biomedical Applications, ACS Appl. Mater. Interfaces, 2020, 12, 45673–45701.
- 13 A. Martins, J. V. Araujo, R. L. Reis and N. M. Neves, Electrospun nanostructured scaffolds for tissue engineering applications, *Nanomedicine*, 2007, 2, 929–942.
- 14 A. Martins, R. L. Reis and N. M. Neves, Electrospinning: processing technique for tissue engineering scaffolding, *Int. Mater. Rev.*, 2008, **53**, 257–274.
- 15 S. D. McCullen, S. Ramaswamy, L. I. Clarke and R. E. Gorga, Nanofibrous composites for tissue engineering applications, *Wiley Interdiscip. Rev.: Nanomed. Nanobiotechnol.*, 2009, 1, 369–390.
- 16 J. Diani, Y. P. Liu and K. Gall, Finite strain 3D thermoviscoelastic constitutive model for shape memory polymers, *Polym. Eng. Sci.*, 2006, 46, 486-492.
- 17 A. Greiner and J. H. Wendorff, Electrospinning: A fascinating method for the preparation of ultrathin fibres, *Angew. Chem.*, *Int. Ed.*, 2007, **46**, 5670–5703.
- 18 D. H. Reneker, A. L. Yarin, E. Zussman and H. Xu, Electrospinning of nanofibers from polymer solutions and melts, in *Advances in Applied Mechanics, Vol. 41*, ed. H. Aref and E. VanDerGiessen, Elsevier Academic Press Inc, San Diego, 2007, vol. 41, pp. 43–195.
- 19 N. Bhardwaj and S. C. Kundu, Electrospinning: A fascinating fiber fabrication technique, *Biotechnol. Adv.*, 2010, **28**, 325–347.
- 20 Z. M. Huang, Y. Z. Zhang, M. Kotaki and S. Ramakrishna, A review on polymer nanofibers by electrospinning and their applications in nanocomposites, *Compos. Sci. Technol.*, 2003, **63**, 2223–2253.
- 21 Web of Science. http://apps.webofknowledge.com/.
- 22 Q. Q. Wang, C. K. Curtis, N. M. Thoppey, J. R. Bochinski, R. E. Gorga and L. I. Clarke, Unconfined, melt edge electrospinning from multiple, spontaneous, self-organized polymer jets, *Mater. Res. Express*, 2014, 1.
- 23 M. P. Roman, N. M. Thoppey, R. E. Gorga, J. R. Bochinski and L. I. Clarke, Maximizing Spontaneous Jet Density and Nanofiber Quality in Unconfined Electrospinning: The Role of Interjet Interactions, *Macromolecules*, 2013, 46, 7352–7362.

- 24 N. M. Thoppey, J. R. Bochinski, L. I. Clarke and R. E. Gorga, Unconfined fluid electrospun into high quality nanofibers from a plate edge, *Polymer*, 2010, **51**, 4928–4936.
- 25 N. M. Thoppey, J. R. Bochinski, L. I. Clarke and R. E. Gorga, Edge electrospinning for high throughput production of quality nanofibers, *Nanotechnology*, 2011, 22, 345301.
- 26 N. M. Thoppey, R. E. Gorga, J. R. Bochinski and L. I. Clarke, Effect of Solution Parameters on Spontaneous Jet Formation and Throughput in Edge Electrospinning from a Fluid-Filled Bowl, *Macromolecules*, 2012, 45, 6527–6537.
- 27 N. M. Thoppey, R. E. Gorga, L. I. Clarke and J. R. Bochinski, Control of the electric field-polymer solution interaction by utilizing ultra-conductive fluids, *Polymer*, 2014, 55, 6390–6398.
- 28 A. Frenot and I. S. Chronakis, Polymer nanofibers assembled by electrospinning, *Curr. Opin. Colloid Interface Sci.*, 2003, **8**, 64–75.
- 29 D. W. Hutmacher and P. D. Dalton, Melt Electrospinning, *Chem. Asian J.*, 2011, **6**, 44–56.
- 30 J. N. Hahladakis, C. A. Velis, R. Weber, E. Iacovidou and P. Purnell, An overview of chemical additives present in plastics: Migration, release, fate and environmental impact during their use, disposal and recycling, *J. Hazard. Mater.*, 2018, 344, 179–199.
- 31 M. Natamai Subramanian, *Plastics additives and testing*, Wiley, Hoboken, New Jersey, 2013.
- 32 J. Ma, Q. Zhang, A. Mayo, Z. H. Ni, H. Yi, Y. F. Chen, R. Mu, L. M. Bellan and D. Y. Li, Thermal conductivity of electrospun polyethylene nanofibers, *Nanoscale*, 2015, 7, 16899–16908.
- 33 J. Ma, Q. Zhang, Y. Zhang, L. Zhou, J. K. Yang and Z. H. Ni, A rapid and simple method to draw polyethylene nanofibers with enhanced thermal conductivity, *Appl. Phys. Lett.*, 2016, **109**, 5.
- 34 D. M. Rein, L. Shavit-Hadar, R. L. Khalfin, Y. Cohen, K. Shuster and E. Zussman, Electrospinning of ultrahighmolecular-weight polyethylene nanofibers, *J. Polym. Sci.*, *Part B: Polym. Phys.*, 2007, 45, 766–773.
- 35 S. R. Givens, K. H. Gardner, J. F. Rabolt and D. B. Chase, High-temperature electrospinning of polyethylene microfibers from solution, *Macromolecules*, 2007, **40**, 608–610.
- 36 T. Miloh, B. Spivak and A. L. Yarin, Needleless electrospinning: Electrically driven instability and multiple jetting from the free surface of a spherical liquid layer, *J. Appl. Phys.*, 2009, **106**, 114910.
- 37 P.-G. de Gennes, F. Brochard-Wyart and D. Quere, *Capillarity and Wetting Phenomena*, Springer, New York, 2010.
- 38 P. Potschke, E. Pionteck and H. Stutz, Surface tension, interfacial tension, and morphology in blends of thermoplastic polyurethanes and polyolefins. Part I. Surface tension of melts of TPU model substances and polyolefins, *Polymer*, 2002, **43**, 6965–6972.
- 39 F. J. Higuera, Stationary viscosity-dominated electrified capillary jets, *J. Fluid Mech.*, 2006, **558**, 143–152.
- 40 F. J. Higuera, Numerical computation of the domain of operation of an electrospray of a very viscous liquid, *J. Fluid Mech.*, 2010, **648**, 35–52.

- 41 I. Avramov, Relationship between diffusion, self-diffusion and viscosity, J. Non-Cryst. Solids, 2009, 355, 745-747.
- 42 S. Seki, K. Hayamizu, S. Tsuzuki, K. Takahashi, Y. Ishino, M. Kato, E. Nozaki, H. Watanabe and Y. Umebayashi, Density, Viscosity, Ionic Conductivity, and Self-Diffusion Coefficient of Organic Liquid Electrolytes: Part I. Propylene Carbonate plus Li, Na, Mg and Ca Cation Salts, J. Electrochem. Soc., 2018, 165, A542-A546.
- 43 T. Yamaguchi, E. Nakahara and S. Koda, Quantitative Analysis of Conductivity and Viscosity of Ionic Liquids in Terms of Their Relaxation Times, J. Phys. Chem. B, 2014, 118, 5752-5759.

- 44 B. Subbiah and K. R. Morison, Electrical conductivity of viscous liquid foods, J. Food Eng., 2018, 237, 177-182.
- 45 F. Gómez, J. Bernal, J. Rosales and T. Cordova, Modeling and Simulation of Equivalent Circuits in Description of Biological Systems - A Fractional Calculus Approach, J. Electr. Bioimpedance, 2012, 3, 2-11.
- 46 J. Jacquelin, A Number of Models for CPA Impedances of Conductors and for Relaxation in Non-DeBye Dielectrics, J. Non-Cryst. Solids, 1991, 131, 1080-1083.
- 47 X. M. Qian, N. Y. Gu, Z. L. Cheng, X. R. Yang, E. K. Wang and S. J. Dong, Methods to study the ionic conductivity of polymeric electrolytes using a.c. impedance spectroscopy, J. Solid State Electrochem., 2001, 6, 8-15.